A mathematical description of the flow in a spherical lymph node

Giulia Giantesio[1], Alberto Girelli[2] and Alessandro Musesti[1*]

[1]Dipartimento di Matematica e Fisica, Università Cattolica del Sacro Cuore, Brescia, Italy.
[2]Dipartimento di Matematica e Applicazioni, Università degli Studi di Milano-Bicocca, Italy.

*Corresponding author(s). E-mail(s):
alessandro.musesti@unicatt.it;
Contributing authors: giulia.giantesio@unicatt.it;
a.girelli3@campus.unimib.it;

Abstract

The motion of the lymph has a very important role in the immune system and it is influenced by the porosity of the lymph nodes: more than 90% takes the peripheral path without entering the lymphoid compartment. In this paper, we construct a mathematical model of a lymph node assumed to have a spherical geometry, where the subcapsular sinus is a thin spherical shell near the external wall of the lymph node and the core is a porous material describing the lymphoid compartment. For the mathematical formulation we assume incompressibility and we use Stokes together with Darcy-Brinkman equation for the flow of the lymph. Thanks to the hypothesis of axisymmetric flow with respect to the azimuthal angle and the use of the stream function approach, we find an explicit solution for the fully developed pulsatile flow in terms of Gegenbauer polynomials. A selected set of plots is provided to show the trend of motion in the case of physiological parameters. Then, a finite element simulation is performed and it is compared with the explicit solution.

Keywords: lymph node; Darcy-Brinkman equation; pulsatile flow; spherical domain

1 Introduction

Lymph nodes are organs scattered throughout the lymphatic system which play a vital role in our immune response in breaking down bacteria, viruses and waste; the interstitial fluid (called *lymph* once inside the lymphatic system) is of fundamental importance in doing this since it transports these substances inside the lymph node [1]. The main features of the lymph node from a mechanical point of view are the presence of a porous bulk region (*lymphoid compartment*, LC), surrounded by a thin layer (*subcapsular sinus*, SCS) where the fluid can flow freely. More than 90% of the lymph remains in the SCS, while the remaining part enters into the LC through a conduit system network [2–4] formed by fibroblastic reticular cells (FRC), which is the *parenchyma* of the LN [5]; due to this, LNs are organs with high resistance to flow. The bigger particles cannot enter the conduits formed by FRC and remain in the SCS, where they are confined and filtered by specialized cells of the lymphatic endothelial cells; however, there is some evidence that the selectivity of the FRC network is not based solely on the size of the molecules; indeed, selected macromolecules, such as antibodies, can gain access to the LN parenchyma [6].

Lymph flow inside LNs has an important function; indeed, fluid flow biases macromolecular distribution, enhances ligand expression, aligns extracellular matrix and shapes active mechanisms of cell migration. Fluid flow through endothelial monolayers and FRC networks enhances the expression of chemokines that direct leucocyte localization and migration patterns [7]. Moreover, increased flows enhance proliferation and drug sensitivity in B cell lymphoma [8, 9]. Fluid flow is important to study the tumor metastasis [10] and drug transport [11]. Despite its importance, as far as we know, only few models in the literature try to describe the behavior of the lymph from a mechanical point of view [12–17] or mimicking the LN mechanical properties in a LN-on-a-chip model [10, 18, 19].

In this paper, we propose a mathematical model for the flow of the interstitial fluid in a lymph node. We assume the lymph to be an incompressible fluid similar to water; moreover, we assume a small Reynolds number as a result of the small velocities within the lymph nodes [20], hence we can model the flow into the LC by Darcy-Brinkman equation (due to the high porosity and the time-dependence of the flow [4, 18]), and the flow inside the SCS by Stokes equation. The lymph enters the lymph node from the lymphatic vessels, which have a complex structure formed by one-way valves that prevent retrograde flow and a wall structure composed of sinus-lining cells: such cells control and generate active pulsation of the wall, pumping the lymph from a segment between two valves to another (the segment is called *lymphangion*)[20, 21]. This means that the lymph has a relevant pulsatile behavior, and we take it into account in our model. In Section 2 we describe the behavior of the lymph explicitly in spherical geometry, supposing that the fluid flow inside the lymph node is axisymmetric with respect to the azimuthal angle, so that we can assume a simplified two-dimensional geometry and we can use

the stream function approach [22] to find an explicit solution. We remark that
the solution given in Section 2.1 is quite general and can be used also for other
choices of boundary conditions. Finally, in Section 3 we compare our results
with some finite element simulations obtained using the open source software
FreeFEM [23].

2 Explicit result in a simplified case

Let us model the lymph node (LN) as a spherical region: the subcapsular sinus
(SCS) is a thin spherical shell with radii $R_1 < R_2$ of creeping fluid flowing
near the external wall of the LN, while the lymphoid compartment (LC) is a
sphere of radius R_1 of porous material. We use spherical coordinates (r, θ, ϕ),
where r is the radial distance, θ the polar angle and ϕ the azimuthal angle;
moreover, we suppose axial symmetry with respect to the azimuthal angle ϕ.

Assuming that the lymph, which flows inside the LN, is an incompressible
fluid, and that the Reynolds number is small, we have the equations

$$\begin{cases} \rho_0 \dfrac{\partial \boldsymbol{v}}{\partial t}(r, \theta, t) = -\nabla p(r, \theta, t) + \mu_e \Delta \boldsymbol{v}(r, \theta, t) - \dfrac{\mu}{k} \boldsymbol{v}(r, \theta, t) & r \in [0, R_1] \\ \rho_0 \dfrac{\partial \boldsymbol{v}}{\partial t}(r, \theta, t) = -\nabla p(r, \theta, t) + \mu \Delta \boldsymbol{v}(r, \theta, t) & r \in [R_1, R_2] \\ \operatorname{div} \boldsymbol{v}(r, \theta, t) = 0 \end{cases} \quad (1)$$

where ρ_0 is the constant density, $\boldsymbol{v}$ the velocity, p is the pressure, μ the vis-
cosity of the lymph, μ_e the *effective viscosity*, k the *permeability*. The second
equation in (1) is the *Stokes equation* and describes the motion in the sub-
capsular sinus, the first is the *Darcy-Brinkman equation*, which is used for
modeling the flow in the porous region of the LC, while the last equation mod-
els the incompressibility of the fluid. Here we assume a constant homogeneous
permeability k [4, 18]. The effective viscosity μ_e in general differs from the clas-
sical viscosity μ because μ_e keeps into account the Brinkman correction [24].
Furthermore, assuming that the flow is time periodic with period T, we write
the time dependence of the velocity and of the pressure as a Fourier expansion

$$\boldsymbol{v}(r, \theta, t) = \sum_{m=-\infty}^{\infty} \boldsymbol{v}_m(r, \theta) e^{im\omega t}, \quad p(r, \theta, t) = \sum_{m=-\infty}^{\infty} p_m(r, \theta) e^{im\omega t}, \quad (2)$$

where $\omega = 2\pi/T$.

2.1 Solving the equations

Now we want to compute the general solution of system (1) in terms of
the Fourier expansion (2). Here we try to be as general as possible, without
imposing any boundary condition, so that out solution can be used in sev-
eral situations. We will deal with suitable boundary conditions for our specific
problem in Section 2.3.

By using (2), system (1) becomes

$$
\begin{cases}
\Delta \boldsymbol{v}_m(r,\theta) - \left(\dfrac{\mu}{k\mu_e} + \dfrac{im\omega\rho_0}{\mu_e} \right) \boldsymbol{v}_m(r,\theta) = \dfrac{1}{\mu_e}\nabla p_m(r,\theta) & \text{in } [0, R_1], \\[2mm]
\Delta \boldsymbol{v}_m(r,\theta) - \dfrac{im\omega\rho_0}{\mu}\boldsymbol{v}_m(r,\theta) = \dfrac{1}{\mu}\nabla p_m(r,\theta) & \text{in } [R_1, R_2], \\[2mm]
\operatorname{div} \boldsymbol{v}_m(r,\theta) = 0,
\end{cases}
\tag{3}
$$

which can be written in compact form as

$$
\begin{cases}
\Delta \boldsymbol{v}_m(r,\theta) - q_m(r)\boldsymbol{v}_m(r,\theta) = \dfrac{1}{\mu}\nabla p_m(r,\theta) \\[2mm]
\operatorname{div} \boldsymbol{v}_m(r,\theta) = 0,
\end{cases}
\qquad m \in \mathbb{Z},
\tag{4}
$$

where $\mathbb{Z}$ is the set of integers, while q_m is given by

$$
q_m(r) = \begin{cases}
\dfrac{\mu}{k\mu_e} + \dfrac{im\omega\rho_0}{\mu_e} & \text{in } [0, R_1], \\[3mm]
\dfrac{im\omega\rho_0}{\mu} & \text{in } [R_1, R_2].
\end{cases}
\tag{5}
$$

Now, writing $\boldsymbol{v}_m = v_{r,m}\mathbf{e}_r + v_{\theta,m}\mathbf{e}_\theta$, we introduce the *stream function* ψ_m [22] as

$$
v_{r,m}(r,\theta) = -\frac{1}{r^2\sin\theta}\frac{\partial\psi_m}{\partial\theta}, \qquad v_{\theta,m}(r,\theta) = \frac{1}{r\sin\theta}\frac{\partial\psi_m}{\partial r}.
\tag{6}
$$

Moreover, it is useful to perform the change of variable $\zeta := \cos\theta$, so that the previous equations become

$$
v_{r,m}(r,\zeta) = \frac{1}{r^2}\frac{\partial\psi_m}{\partial\zeta}, \qquad v_{\theta,m}(r,\zeta) = \frac{1}{r\sqrt{1-\zeta^2}}\frac{\partial\psi_m}{\partial r}.
\tag{7}
$$

By introducing the operator

$$
\mathrm{E}^2 = \frac{\partial^2}{\partial r^2} + \frac{(1-\zeta^2)}{r^2}\frac{\partial^2}{\partial\zeta^2},
$$

we can rewrite (4) as

$$
\mathrm{E}^2\left(\mathrm{E}^2\,\psi_m(r,\zeta)\right) - q_m(r)\,\mathrm{E}^2\,\psi_m(r,\zeta) = 0, \quad m \in \mathbb{Z},
\tag{8}
$$

while for the pressure we have

$$
\begin{cases}
\dfrac{\partial p_m}{\partial r} = \dfrac{\mu}{r^2}\dfrac{\partial}{\partial\zeta}\left(\left(\mathrm{E}^2 - q_m(r)\right)\psi_m\right) \\[3mm]
\dfrac{\partial p_m}{\partial\zeta} = -\dfrac{\mu}{1-\zeta^2}\dfrac{\partial}{\partial r}\left(\left(\mathrm{E}^2 - q_m(r)\right)\psi_m\right)
\end{cases}
\qquad m \in \mathbb{Z}.
\tag{9}
$$

Focusing on the case $m \neq 0$, we have that the solution can be written as

$$\psi_m(r, \zeta) = \psi_{1,m}(r, \zeta) + \psi_{2,m}(r, \zeta),$$

where

$$E^2 \psi_{1,m}(r, \zeta) = 0, \quad E^2 \psi_{2,m}(r, \zeta) - q_m(r)\psi_{2,m}(r, \zeta) = 0. \tag{10}$$

We can now solve (10): by using the separation of variables

$$\psi_{1,m}(r, \zeta) = R(r)Z(\zeta), \tag{11}$$

substituting in the first equation of (10) we get

$$\frac{r^2}{R} \frac{d^2 R}{dr^2} + \frac{1 - \zeta^2}{Z} \frac{d^2 Z}{d\zeta^2} = 0. \tag{12}$$

As the first term of (12) depends only on r and the second term only on ζ, the two have to be constant, say $n(n-1)$ with $n \in \mathbb{N}$ [25], where $\mathbb{N}$ is the set of natural numbers. Hence (12) becomes

$$r^2 \frac{d^2 R}{dr^2} - n(n-1)R = 0, \tag{13}$$

$$\left(1 - \zeta^2\right) \frac{d^2 Z}{d\zeta^2} + n(n-1)Z = 0. \tag{14}$$

The solution of (13) is given by

$$R^{(n)}(r) = A^{(n)} r^n + B^{(n)} r^{1-n}, \tag{15}$$

for some constants $A^{(n)}, B^{(n)}$, while (14) is the *Gegenbauer equation*, whose solutions are the *Gegenbauer polynomials* G_n, H_n with order $-1/2$, of the first and second kind, respectively. Hence the solution of the first equation of (10) becomes

$$\psi_{1,m} = \sum_{n=0}^{\infty} \left[\left(A_m^{(n)} r^n + B_m^{(n)} r^{1-n} \right) G_n(\zeta) + \left(C_m^{(n)} r^n + D_m^{(n)} r^{1-n} \right) H_n(\zeta) \right]$$

for some constants $A_m^{(n)}, B_m^{(n)}, C_m^{(n)}, D_m^{(n)}$. Since H_n is not smooth in $\zeta = \pm 1$ and G_0, G_1 lead to an infinite tangential velocity, the solution simplifies as

$$\psi_{1,m}(r, \zeta) = \sum_{n=2}^{\infty} \left(A_m^{(n)} r^n + B_m^{(n)} r^{1-n} \right) G_n(\zeta), \tag{16}$$

for some constants $A_m^{(n)}, B_m^{(n)}$.

The second equation of (10) is

$$\frac{\partial^2 \psi_{2,m}}{\partial r^2} + \frac{1-\zeta^2}{r^2}\frac{\partial^2 \psi_{2,m}}{\partial \zeta^2} - q_m(r)\psi_{2,m} = 0 \qquad (17)$$

and, using again the separation of variables,

$$\psi_{2,m}(r,\zeta) = R(r)Z(\zeta),$$

by a similar procedure as before, we obtain

$$\frac{d^2 R}{dr^2} - q_m R - \frac{n(n-1)}{r^2}R = 0, \qquad (18)$$

$$(1-\zeta^2)\frac{d^2 Z}{d\zeta^2} + n(n-1)Z = 0. \qquad (19)$$

Equation (18) is a Bessel equation, hence the solution can be written as

$$R^{(n)}(r) = \alpha^{(n)}\sqrt{r}J_{n-\frac{1}{2}}\left(-i\sqrt{q_m}r\right) + \beta^{(n)}\sqrt{r}Y_{n-\frac{1}{2}}\left(-i\sqrt{q_m}r\right),$$

where J_s, Y_s are the *Bessel functions of the first and second kind*, respectively. Equation (19) is the same Gegenbauer equation as (14), hence the solution of (17) is given by

$$\psi_{2,m} = \sum_{n=2}^{\infty}\left[\alpha_m^{(n)}\sqrt{r}J_{n-\frac{1}{2}}\left(-i\sqrt{q_m}r\right) + \beta_m^{(n)}\sqrt{r}Y_{n-\frac{1}{2}}\left(-i\sqrt{q_m}r\right)\right]G_n(\zeta),$$

and the general solution $\psi_m = \psi_{1,m} + \psi_{2,m}$ is

$$\psi_m(r,\zeta) = \sum_{n=2}^{\infty}\left[A_m^{(n)}r^n + B_m^{(n)}r^{1-n} + \alpha_m^{(n)}\sqrt{r}J_{n-\frac{1}{2}}\left(-i\sqrt{q_m}r\right)\right.$$
$$\left. + \beta_m^{(n)}\sqrt{r}Y_{n-\frac{1}{2}}\left(-i\sqrt{q_m}r\right)\right]G_n(\zeta). \quad (20)$$

Now we want to employ the definition of q_m, so that we have to distinguish between the Stokes and the Darcy-Brinkman case. Let us denote with $A_m^{(n)}$, $B_m^{(n)}$, $\alpha_m^{(n)}$, $\beta_m^{(n)}$ the constants of the Stokes case ($R_1 \le r \le R_2$) and with $\bar{A}_m^{(n)}$, $\bar{B}_m^{(n)}$, $\bar{\alpha}_m^{(n)}$, $\bar{\beta}_m^{(n)}$ those of the Darcy-Brinkman case ($0 \le r \le R_1$). Using (5), we obtain, for any $m \ne 0$,

$$\psi_m^S(r,\zeta) = \sum_{n=2}^{\infty}\left[A_m^{(n)}r^n + B_m^{(n)}r^{1-n} + \alpha_m^{(n)}\sqrt{r}J_{n-\frac{1}{2}}\left(-i\sqrt{\frac{i\rho_0 m\omega}{\mu}}r\right)\right.$$
$$\left. + \beta_m^{(n)}\sqrt{r}Y_{n-\frac{1}{2}}\left(-i\sqrt{\frac{i\rho_0 m\omega}{\mu}}r\right)\right]G_n(\zeta), \qquad (21)$$

$$\psi_m^B(r,\zeta) = \sum_{n=2}^{\infty} \left[\bar{A}_m^{(n)} r^n + \bar{\alpha}_m^{(n)} \sqrt{r} J_{n-\frac{1}{2}} \left(-i\sqrt{\frac{i\rho_0 m\omega}{\mu_e} + \frac{\mu}{\mu_e k}} r \right) \right] G_n(\zeta), \quad (22)$$

where the superscript S denotes the Stokes case and B the Darcy-Brinkman case, and we used the fact that $r = 0$ is in the domain of ψ^B, so that $\bar{B}_m^{(n)} = \bar{\beta}_m^{(n)} = 0$ in view of the non degeneracy of the solution.

Regarding the pressure, we use (9) to obtain

$$p_m^S(r,\zeta) = C_m^S + im\omega\rho_0 \sum_{n=2}^{\infty} \left[\frac{A_m^{(n)}}{n-1} r^{n-1} - \frac{B_m^{(n)}}{n} r^{-n} \right] P_{n-1}(\zeta) \quad (23)$$

in the Stokes case, and

$$p_m^B(r,\zeta) = C_m^B + \left(im\omega\rho_0 + \frac{\mu}{k} \right) \sum_{n=2}^{\infty} \frac{\bar{A}_m^{(n)}}{n-1} r^{n-1} P_{n-1}(\zeta) \quad (24)$$

in the Darcy-Brinkman case, where P_n are the Legendre polynomials of the first kind.

For $m = 0$ we get the well-known steady solution of the Stokes equation

$$\begin{cases} \psi_0^S = \sum_{n=2}^{\infty} \left(A_0^{(n)} r^n + B_0^{(n)} r^{1-n} + C_0^{(n)} r^{n+2} + D_0^{(n)} r^{-n+3} \right) G_n(\zeta), \\ p_0^S = C_0^S - \mu \sum_{n=2}^{\infty} \left[\frac{2(2n+1)}{n-1} C_0^{(n)} r^{n-1} + \frac{2(2n-3)}{n} D_0^{(n)} r^{-n} \right] P_{n-1}(\zeta) \end{cases} \quad (25)$$

and for the Darcy-Brinkman equation we have

$$\begin{cases} \psi_0^B = \sum_{n=2}^{\infty} \left[\bar{A}_0^{(n)} r^n + \bar{B}_0^{(n)} \sqrt{r} J_{n-\frac{1}{2}} \left(-i\sqrt{\frac{\mu}{\mu_e k}} r \right) \right] G_n(\zeta), \\ p_0^B = C_0^B + \frac{\mu}{k} \sum_{n=2}^{\infty} \left[\frac{\bar{A}_0^{(n)}}{n-1} r^{n-1} \right] P_{n-1}(\zeta). \end{cases} \quad (26)$$

2.2 Geometrical and physiological parameters

We use an idealized spherical geometry based on the data obtained from a murine (popliteal) lymph node: the radius is $R_2 = 0.5\,\text{mm}$, the subcapsular sinus (SCS) thickness is $h = 10\,\mu\text{m}$, the afferent and efferent lymphatic vessels have the same radius $R_{LV} = 40\,\mu\text{m}$ [10, 13, 18, 26–29]. With these data, we have that more than 90% of the lymph takes the peripheral path without entering the LC in a pulsation cycle [13, 30, 31].

The inlet and outlet conditions are imposed in the upper and lower lymphatic vessel (near $\theta = 0$ and $\theta = \pi$, respectively) as a pulsatile flow of the

Variable name	Value	Description
R_2	$0.5\,\text{mm}$	external radius
h	$10\,\mu\text{m}$	height of SCS
R_1	$R_2 - h$	internal radius
R_{LV}	$40\,\mu\text{m}$	lymphatic vessel radius
μ	$1\,\text{mg}/(\text{mm s})$	viscosity
ϕ	0.75	porosity
μ_e	$\frac{\mu}{\phi}$	effective viscosity
ρ	$1\,\text{mg}/\text{mm}^3$	density
β	0.7	stress jump
k	$3.84 \times 10^{-9}\,\text{mm}^2$	permeability
L	$10^{-3}\,\text{mm}^3/\text{s}$	maximum lymph fluid mean flow

Table 1 Physiological parameters of Section 2.2.

form
$$v_{in}(\theta, t) = \frac{L}{\pi R_{LV}^2} f(t) H(\cos\theta), \tag{27}$$
where L is the maximum lymph mean flow of the inlet lymphatic vessel. Here we assume $L = 10^{-3}\,\text{mm}^3/\text{s}$, as measured in [32], and $f(t)$ is a periodic function. The function H is given by

$$H(\zeta) = \begin{cases} 1 & \zeta \in [-1, -1 + \zeta_0] \\ 0 & \zeta \in (-1 + \zeta_0, 1 - \zeta_0) \\ -1 & \zeta \in [1 - \zeta_0, 1], \end{cases} \tag{28}$$

where the constant $0 < \zeta_0 < 1$ describes the inlet and outlet regions, and is given by
$$\zeta_0 = \cos\left[\arcsin\left(\frac{R_{LV}}{\sqrt{R_{LV}^2 + R_2^2}}\right)\right] = \frac{R_2}{\sqrt{R_{LV}^2 + R_2^2}}.$$
Notice that we are assuming that the inlet and outlet velocities are the same.

The lymph is modeled as an incompressible Newtonian fluid similar to water [20] with viscosity $\mu = 1\,\text{mg}/(\text{mm s})$ and density $\rho_0 = 1\,\text{mg}/\text{mm}^3$. The permeability is considered homogeneous [4] with value $k = 3.84 \times 10^{-9}\,\text{mm}^2$ [18]. The effective viscosity is taken as $\mu_e = \frac{\mu}{\phi}$ [33, 34], where ϕ is the *porosity* taken as $\phi = 0.75$ [18]. The parameters are summarized in Table 1.

2.3 Boundary conditions

We now want to impose suitable boundary conditions to our general solution. We give a *Dirichlet condition* at the external boundary and the *Ochoa-Tapia boundary conditions* [33, 35] at the interface between the porous zone LC and the free-fluid region SCS. In this way we can close the problem and find a unique solution.

More precisely, we will assume the *no-slip condition* for the velocity on R_2, except near $\theta = 0, \pi$, where we impose the inlet/outlet flow (27). For simplicity, given the small diameter of the afferent/efferent lymphatic vessel, we impose the inlet/outlet condition only for the radial velocity v_r, but we could use the same procedure to impose boundary condition for v_θ too. For the boundary conditions on the internal radius R_1, the Ochoa-Tapia boundary conditions imply the continuity of radial and tangential velocity, the continuity of the normal stress tensor and a jump-condition on the shear stress.

Thanks to the above conditions, we can determine for every n the six unknown constants in equations (21)-(22). For the sake of brevity, we rewrite the stream functions as

$$\psi_m^{S/B}(r,\zeta) = \sum_{n=2}^{\infty} \tilde{\psi}_{m,n}^{S/B}(r)G_n(\zeta), \quad p_m^{S/B} = \sum_{n=2}^{\infty} \tilde{p}_{m,n}^{S/B}(r)P_{n-1}(\zeta).$$

Expanding the step function $H(\zeta)$ in (28) in terms of Legendre polynomials, we get

$$H(\zeta) = \sum_{n=2}^{\infty} b_{n-1}P_{n-1}(\zeta), \tag{29}$$

where

$$b_n = \frac{2n+1}{2} \int_{-1}^{1} H(\zeta)P_n(\zeta)d\zeta = \frac{2n+1}{2} \left(\int_{-1}^{-1+\zeta_0} P_n(\zeta)d\zeta - \int_{1-\zeta_0}^{1} P_n(\zeta)d\zeta \right)$$

and we kept into account that $b_0 = 0$ since H is an odd function.

To impose the boundary condition, we need to expand in Fourier series the time dependence of (27), as we did in (2). Writing

$$f(t) = \sum_{m=-\infty}^{\infty} f_m e^{im\omega t},$$

it follows that

$$v_{in}(\zeta, t) = \frac{L}{\pi R_{LV}^2} H(\zeta) \sum_{m=-\infty}^{\infty} f_m e^{im\omega t}$$

$$= \frac{L}{\pi R_{LV}^2} \sum_{n=2}^{\infty} \sum_{m=-\infty}^{\infty} b_{n-1} P_{n-1}(\zeta) f_m e^{im\omega t}.$$

Now we impose the boundary condition $v_r(R_2, \zeta, t) = v_{in}(\zeta, t)$: recalling the relation $G_n'(\zeta) = -P_{n-1}(\zeta)$, by (7)$_1$ we obtain

$$\frac{1}{R_2^2}\psi_m^S(R_2, \zeta) = -\frac{L}{\pi R_{LV}^2} \sum_{n=2}^{\infty} b_{n-1}G_n(\zeta), \tag{30}$$

whence

$$\tilde{\psi}_{m,n}^S(R_2) = -\frac{R_2^2 L}{\pi R_{LV}^2} b_{n-1} f_m \tag{31}$$

for any $m \in \mathbb{Z}$ and $n \geq 2$, where we used the linear independence of the Gegenbauer polynomials.

By the no-slip boundary condition on v_θ, recalling $(7)_2$ it follows that

$$\frac{\partial \psi_{m,n}^S}{\partial r}(R_2, \zeta) = 0 \quad \Rightarrow \quad \frac{\partial \tilde{\psi}_{m,n}^S}{\partial r}(R_2) = 0, \tag{32}$$

where we used again the linear independence of the Gegenbauer polynomials.

We now write in terms of the stream function the Ochoa-Tapia boundary conditions on the internal radius R_1 [36], using the linear independence of Legendre and Gegenbauer polynomials:

- Continuity of v_r:

$$v_{r,m}^S(R_1, \zeta) = v_{r,m}^B(R_1, \zeta) \quad \Rightarrow \quad \tilde{\psi}_{m,n}^S(R_1) = \tilde{\psi}_{m,n}^B(R_1). \tag{33}$$

- Continuity of v_θ:

$$v_{\theta,m}^S(R_1, \zeta) = v_{\theta,m}^B(R_1, \zeta) \quad \Rightarrow \quad \frac{\partial \tilde{\psi}_{m,n}^S}{\partial r}(R_1) = \frac{\partial \tilde{\psi}_{m,n}^B}{\partial r}(R_1). \tag{34}$$

- Continuity of normal stress:

$$T_{rr,m}^S(R_1, \zeta) = T_{rr,m}^B(R_1, \zeta),$$

where

$$T_{rr,m} = -p_m + 2\mu \frac{\partial v_{r,m}}{\partial r}; \tag{35}$$

we can write this condition as

$$-\tilde{p}_{m,n}^S(R_1, \zeta) + 4\mu \frac{1}{R_1^3} \tilde{\psi}_{m,n}^S(R_1, \zeta) - 2\mu \frac{1}{R_1^2} \frac{\partial \tilde{\psi}_{m,n}^S}{\partial r}(R_1, \zeta) =$$

$$= -\tilde{p}_{m,n}^B(R_1, \zeta) + 4\mu_e \frac{1}{R_1^3} \tilde{\psi}_{m,n}^B(R_1, \zeta) - 2\mu_e \frac{1}{R_1^2} \frac{\partial \tilde{\psi}_{m,n}^B}{\partial r}(R_1, \zeta). \tag{36}$$

- The stress jump condition:

$$T_{r\theta,m}^S(R_1, \zeta) - T_{r\theta,m}^B(R_1, \zeta) = \frac{\beta\mu}{\sqrt{k}} v_{\theta,m}^B(R_1, \zeta), \tag{37}$$

where β is the *slip constant* which has to be estimated experimentally. Since the expression of the shear stress is

$$T_{r\theta,m} = \mu \left[\frac{1}{r} \frac{\partial v_{r,m}}{\partial \theta} - \frac{v_{\theta,m}}{r} + \frac{\partial v_{\theta,m}}{\partial r} \right], \tag{38}$$

in the term $\frac{\partial v_{r,m}}{\partial \theta} = -\sqrt{1-\zeta^2} \frac{\partial v_{r,m}}{\partial \zeta}$ there is a second derivative of the Gegenbauer polynomials, so that we need the following property [37, 38]:

$$G_n''(\zeta) = -\frac{n(n-1)}{1-\zeta^2} G_n(\zeta). \tag{39}$$

Hence we have:

$$\frac{\partial v_{r,m}}{\partial \theta} = -\sqrt{1-\zeta^2} \frac{1}{r^2} \frac{\partial^2 \psi_m}{\partial \zeta^2}$$

$$= -\frac{\sqrt{1-\zeta^2}}{r^2} \sum_{n=2}^{\infty} \tilde{\psi}_{m,n}(r) G_n''(\zeta) = \frac{\sqrt{1-\zeta^2}}{r^2} \sum_{n=2}^{\infty} n(n-1) \tilde{\psi}_{m,n}(r) G_n(\zeta).$$

After some computations, eq. (37) can be written as

$$\mu \left[\frac{n(n-1)}{R_1^3} \tilde{\psi}_m^S(R_1) - \frac{2}{R_1^2} \frac{\partial \tilde{\psi}_{m,n}^S}{\partial r}(R_1) + \frac{1}{R_1} \frac{\partial^2 \tilde{\psi}_{m,n}^S}{\partial r^2}(R_1) \right]$$

$$- \mu_e \left[\frac{n(n-1)}{R_1^3} \tilde{\psi}_{m,n}^B(R_1) - \frac{2}{R_1^2} \frac{\partial \tilde{\psi}_{m,n}^B}{\partial r}(R_1) + \frac{1}{R_1} \frac{\partial^2 \tilde{\psi}_{m,n}^B}{\partial r^2}(R_1) \right]$$

$$= \frac{\beta \mu}{\sqrt{k}} \frac{1}{R_1} \frac{\partial \tilde{\psi}_{m,n}^B}{\partial r}(R_1). \tag{40}$$

From (31)–(34), (36) and (40), for every $m \in \mathbb{Z}$ and $n \geq 2$ we obtain a linear system in the unknowns $(A_m^{(n)}, B_m^{(n)}, \alpha_m^{(n)}, \beta_m^{(n)}, \bar{A}_m^{(n)}, \bar{\alpha}_m^{(n)})$, which are the constants of integration of eqs. (21)-(22), and the same holds for the steady case when $m = 0$ in the unknowns $(A_0^{(n)}, B_0^{(n)}, C_0^{(n)}, D_0^{(n)}, \bar{A}_0^{(n)}, \bar{B}_0^{(n)})$ which are the constants of integration of eqs. $(25)_1$–$(26)_1$.

Moreover, we fix the value of the pressure in one point to find the constants in equation (23)–(25) and have a physiological pressure value. By (36), it follows that $C_m^S = C_m^B$ and $C_0^B = C_0^S$. We fix the pressure (with respect to time) at the exit point $(r, \zeta) = (R_2, -1)$ by using the same time function of (27), that is,

$$p(t) = \bar{p} f(t) = \bar{p} \sum_{m=-\infty}^{\infty} f_m e^{im\omega t}.$$
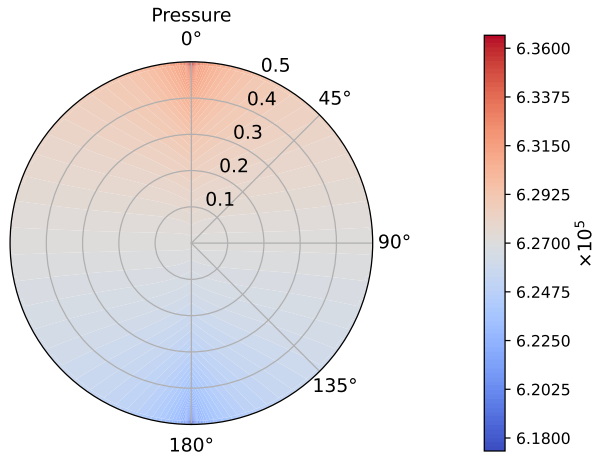
Fig. 1 Pressure distribution in mPa with fixed pressure $p = 6.18 \times 10^5$ mPa at the outlet.

Hence we can find the pressure constants by imposing

$$p_m^S(R_2, -1) = \bar{p} f_m, \quad m \in \mathbb{Z}$$

where $p_m^S(r, \zeta)$ is given in (23) for $m \neq 0$, and in $(25)_2$ for $m = 0$.

2.4 Explicit results

This section is devoted to show some plots related to the explicit solution and to make some considerations about the proposed model.

Following [39], we choose a time function of the form

$$f(t) = \frac{1 - \cos \pi t}{2}. \tag{41}$$

We notice that in this case the period of a pulsatile flow in the lymph node is 2 s, hence $\omega = \pi$, and $f_m = 0$ for $m \neq -1, 0, 1$.

In this model we do not take into account the inhibition and the autoregulation of the contractions in the lymphangion, given by several factors like shear stress and pressure [20, 40]; a further extension of this model can be the coupling with a lymphangion model for taking into account these phenomena.

In Figure 1, we plot the pressure distribution in the LN with the fixed constant $\bar{p} = 6.18 \times 10^5$ mPa (corresponding to the lower limit of the pressure found in [41]); as we can see, the values of the pressure belong to the range given in that paper and, due to the incompressibility of the flow, the pressure translates from a higher value in the inlet zone to a lower value in the outlet zone. We can choose to fix any pressure at the outlet, and we have the same
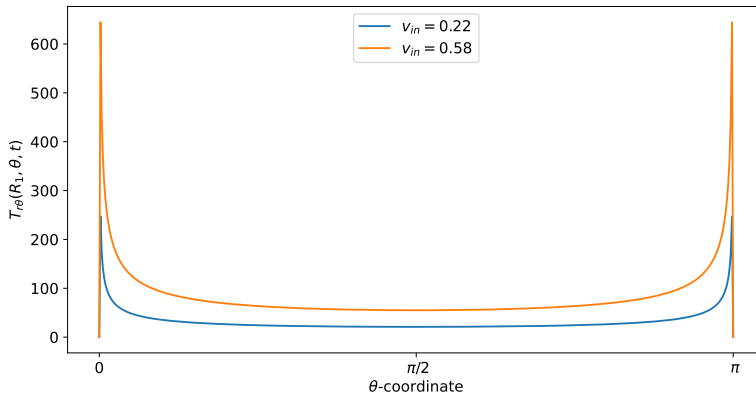
Fig. 2 Shear stress $T_{r\theta}(r,\theta,t)$ in mPa with respect to the polar angle ($\theta = 0$ near the inlet flow and $\theta = \pi$ near the outlet flow) calculated at $t = 1\,$s and in the internal radius R_1 with different boundary velocities in mm/s (where $v_{in} \approx 0.22$ corresponds to $L = 10^{-3}\,\mathrm{mm}^3/\mathrm{s}$ and $v_{in} \approx 0.58$ corresponds to $L = 2.2 \times 10^{-3}\,\mathrm{mm}^3/\mathrm{s}$).

pressure distribution with different values (for example with the fixed pressure of $\bar{p} = 4 \times 10^5\,$mPa $\approx 3\,$mmHg as in [13]).

Figure 2 provides the Stokes shear stress given by the formula:

$$T_{r\theta} = \sum_{m\in\{-1,0,1\}} \mu \left[\frac{1}{r}\frac{\partial v_{r,m}}{\partial \theta} - \frac{v_{\theta,m}}{r} + \frac{\partial v_{\theta,m}}{\partial r} \right] e^{im\pi t},$$

(in mPa) at time $t = 1\,$s, where we have the maximum value of the velocity (and, consequently, of the shear stress) and radius $r = R_1$ (this is the shear stress at the exterior of the LC). We plot the shear stress value with two different boundary velocities: $v_{in} \approx 0.22$ corresponds to the physiological value of $L = 10^{-3}\,\mathrm{mm}^3/\mathrm{s}$, given in Table 1, found in [32], and $v_{in} \approx 0.58$ appears in [13]. As we can see, the shear stress is similar to the one reported in [10, 13]; that is, higher near the inlet flow and lower near $\theta = \frac{\pi}{2}$. The same behavior occurs in the velocity too (see Figure 3). This trend is interesting because the cell adhesion to the exterior of the LC is proportional to the shear stress [10], hence the majority of the cells adhere (and then enter in the LC) near the inlet zone of the lymphatic vessel. Indeed, in our model the inlet shear stress is the same as the outlet one due to the choice of the same inlet/outlet velocity and the incompressibility of the fluid; however, usually a part of the lymph enters in the blood capillaries in the LC [30, 31], so that the shear stress in the outer zone reduces.

As we can see in Figure 3 and in Figure 4, for $\theta > 0$ the tangential component $\boldsymbol{v}_\theta$ of the velocity in the SCS is the larger one. From the first picture in Figure 3 one can see that the fluid flow in the porous medium is flat and starts
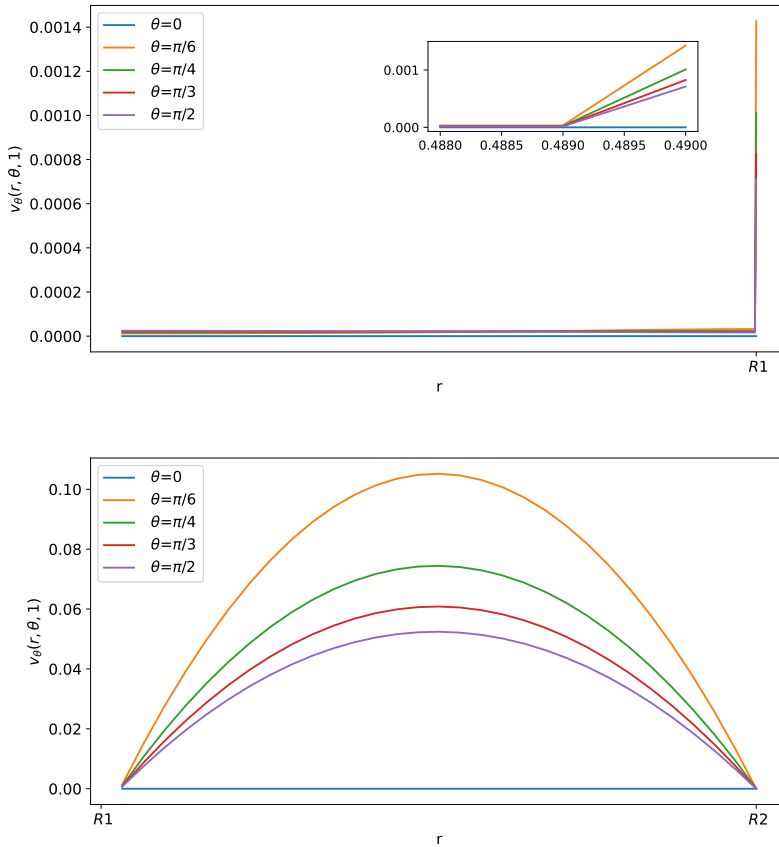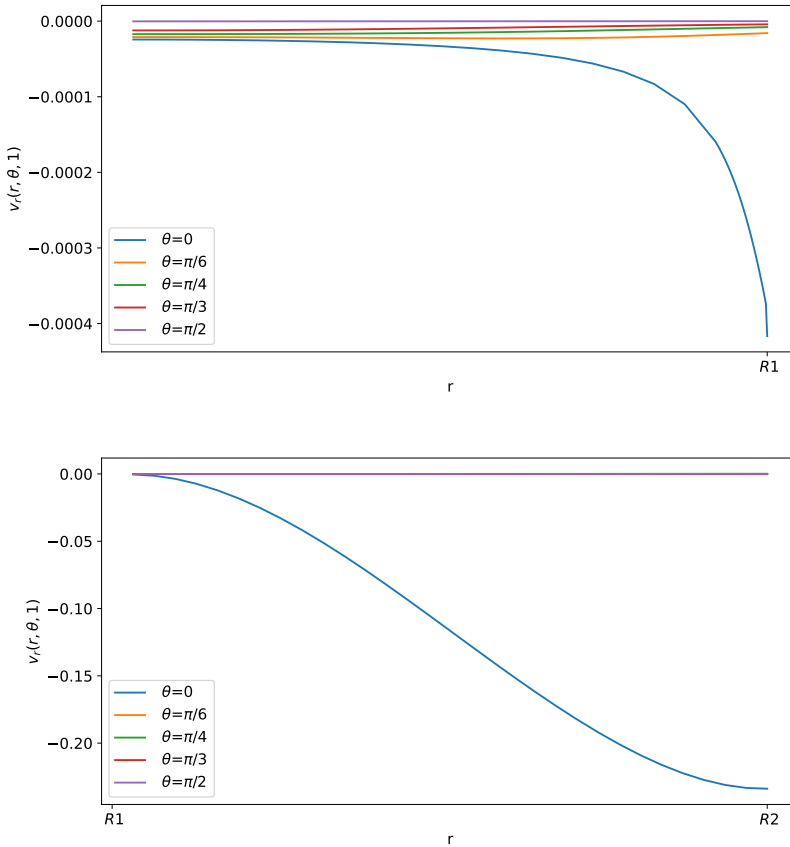
Fig. 3 Tangential component of the velocity in mm/s with respect to the radius at different angles at $t = 1\,\mathrm{s}$. The first picture corresponds to the tangential velocity in the LC (porous part), and the second corresponds to the tangential velocity in the SCS (free-fluid region).

increasing near the interface that connects the LC to the SCS, showing a non-differentiable point due to the Ochoa-Tapia boundary conditions (indeed, we do not impose the continuity of the derivative of $\boldsymbol{v}_\theta$).

3 Numerical simulation

The explicit model found in the previous section uses several simplifications. In this section we propose some numerical simulations to describe a more general fluid flow in a lymph node.

We define two different domains and we call Ω^S the domain of the SCS in which we have the Stokes equation, and Ω^B the LC domain in which we have the Darcy-Brinkman equation. The boundaries of the domain are $\partial\Omega^S = \Gamma_D^S \cup \Gamma_N^S$, where Γ_D^S is the part of the boundary with Dirichlet boundary

Fig. 4 Normal component of the velocity in mm/s with respect to the radius at different angles at $t = 1\,\mathrm{s}$.

condition and Γ_N^S is the one with the Neumann boundary condition and for the domain Ω^B are $\partial\Omega^B = \Gamma_D^B \cup \Gamma_N^B$, where Γ_D^B is the part of the boundary with Dirichlet boundary condition and Γ_N^B is the one with the Neumann boundary condition. We call the boundary interface of the two domains $\Gamma = \partial\Omega^S \cap \partial\Omega^B$. We define the normal $\boldsymbol{n}$ at the interface Γ as the external normal to Ω^B. Moreover, we define the spaces $W^I = \{\boldsymbol{w} \in H^1(\Omega^I) : \boldsymbol{w}_{\Gamma_D} = 0\}$, $W_g^I = \{\boldsymbol{v} \in H^1(\Omega^I) : \boldsymbol{v}_{\Gamma_D} = g\}$, $Q^I = \{q \in L^2(\Omega^I), \text{ with } \int_{\Omega^I} q = 0 \text{ if } \Gamma_D = \partial\Omega^I\}$, where $I = S, B$.

The weak formulation of our problem is (supposing a constant density $\rho = \rho_0$ and viscosity $\nu = \mu/\rho_0$): find $\boldsymbol{v} \in W_g^S$, $p \in Q^S$, $\boldsymbol{v}_b \in W_g^B$ and $p_b \in Q^B$ such that

$$\int_{\Omega^S} \frac{\partial \boldsymbol{v}}{\partial t} \cdot \boldsymbol{w} dV - \frac{1}{\rho_0} \int_{\Omega^S} p \operatorname{div} \boldsymbol{w} dV + \nu \int_{\Omega^S} \mathbf{D}(\boldsymbol{v}) : \mathbf{D}(\boldsymbol{w}) dV + \frac{1}{\rho_0} \int_{\Gamma_N^S} \mathbf{T}\boldsymbol{w} \cdot \boldsymbol{n} dS +$$

$$+ \int_{\Omega^B} \frac{\partial \boldsymbol{v}_b}{\partial t} \cdot \boldsymbol{w}_b dV - \frac{1}{\rho_0} \int_{\Omega^B} p_b \operatorname{div} \boldsymbol{w}_b dV + \nu_e \int_{\Omega^B} \mathbf{D}(\boldsymbol{v}_b) : \mathbf{D}(\boldsymbol{w}_b) dV -$$

$$- \frac{1}{\rho_0} \int_{\Gamma_N^B} \mathbf{T}_e \boldsymbol{w}_b \cdot \boldsymbol{n} dS + \nu \int_{\Omega^B} \mathbf{K}^{-1} \boldsymbol{v}_b \cdot \boldsymbol{w}_b dV + \int_{\Omega^S} \operatorname{div} \boldsymbol{v} q dV + \int_{\Omega^B} \operatorname{div} \boldsymbol{v}_b q_b dV = 0,$$

$$(42)$$

for all $\boldsymbol{w} \in W_g^S$, $\boldsymbol{w}_b \in W_g^B$ such that $\boldsymbol{w} = \boldsymbol{w}_b$ on Γ, and for all $q \in Q^S$ and $q_b \in Q^B$. In equation (42) we have that $\boldsymbol{v}$ is the *velocity* in Ω^S, $p \in Q$ is the *pressure* in Ω^S, $\boldsymbol{v}_b$ is the *velocity* in Ω^B, $p_b \in Q$ is the pressure in Ω^B, $\mathbf{D}(\boldsymbol{v}) = 1/2(\nabla \boldsymbol{v} + \nabla \boldsymbol{v}^T)$, $\mathbf{T} = -p\mathbf{I} + \mu \left[\nabla \boldsymbol{v} + \nabla \boldsymbol{v}^T \right]$, $\nu_e = \mu_e/\rho_0$, $\mathbf{K}$ is the *permeability tensor* (in the case of Section 2, $\mathbf{K} = k\mathbf{I}$), $\mathbf{T}_e = -p_b\mathbf{I} + \mu_e \left[\nabla \boldsymbol{v}_b + \nabla \boldsymbol{v}_b^T \right]$.

Now we want to write the weak formulation for the boundary condition 2.3; we have that the continuity of the velocity is verified automatically, and, for the stress-jump condition, we have [34] (on the interface Γ):

$$\int_\Gamma \mathbf{T} \boldsymbol{w} \cdot \boldsymbol{n} dS - \int_\Gamma \mathbf{T}_e \boldsymbol{w} \cdot \boldsymbol{n} dS = \int_\Gamma \mu \mathbf{B} \sqrt{\mathbf{K}^{-1}} \boldsymbol{v}_b \cdot \boldsymbol{w} dS,$$

where $\mathbf{B}$ is the *slip tensor* (in the case of Section 2.3, $\mathbf{B} = \beta\mathbf{I}$).

The boundary conditions in the external wall (inlet condition and no-slip boundary condition) are imposed by the penalty method. Moreover, we add the Grad-div stabilization terms

$$\gamma_1 \int_{\Omega^{S/B}} \operatorname{div} \boldsymbol{v} \cdot \operatorname{div} \boldsymbol{w} dV + \gamma_2 \int_{\Omega^{S/B}} \operatorname{div} \left(\frac{\partial \boldsymbol{v}}{\partial t} \right) \cdot \operatorname{div} \boldsymbol{w} dV$$

in either Stokes and Darcy-Brinkman domains [42–45]. Thanks to this stabilization term, we have the stability for the Darcy-Brinkman equation (see [46]). For the numerical discretization, we use a BDF2 method for the time discretization, instead, we use $\mathbb{P}_k^d - \mathbb{P}_k$ element pairs (where k is the polynomials order and d is the dimension) with the Brezzi-Pitkäranta stabilization, which consists in adding the term $\epsilon \int_{\Omega^S} \nabla p \cdot \nabla q dV + \epsilon \int_{\Omega^B} \nabla p_b \cdot \nabla q_b dV$ to the discretization of the equation (42), with $\epsilon \approx h_T^2$, where h_T is the maximum diameter of the triangle of the finite element triangulation. The weak formulation here proposed has been implemented using the open source software FreeFEM.

3.1 Numerical Test

In this section we want to qualitatively compare the results obtained with the numerical simulation with the explicit results exposed in Section 2. For that, we use the same geometry and parameters exhibited in Section 2.2; hence, in the external boundary we will impose only Dirichlet boundary condition (Γ_N is empty), subdivided as $\Gamma_D = \Gamma_{\text{in}} \cup \Gamma_{\text{out}} \cup \Gamma_{\text{BC}}$, where we are imposing the inlet and the outlet flow in Γ_{in} and Γ_{out}, respectively, given by the equation (27) with $L = 10^{-3} \, \text{mm}^3/\text{s}$, and the no-slip boundary condition in Γ_{BC}. The
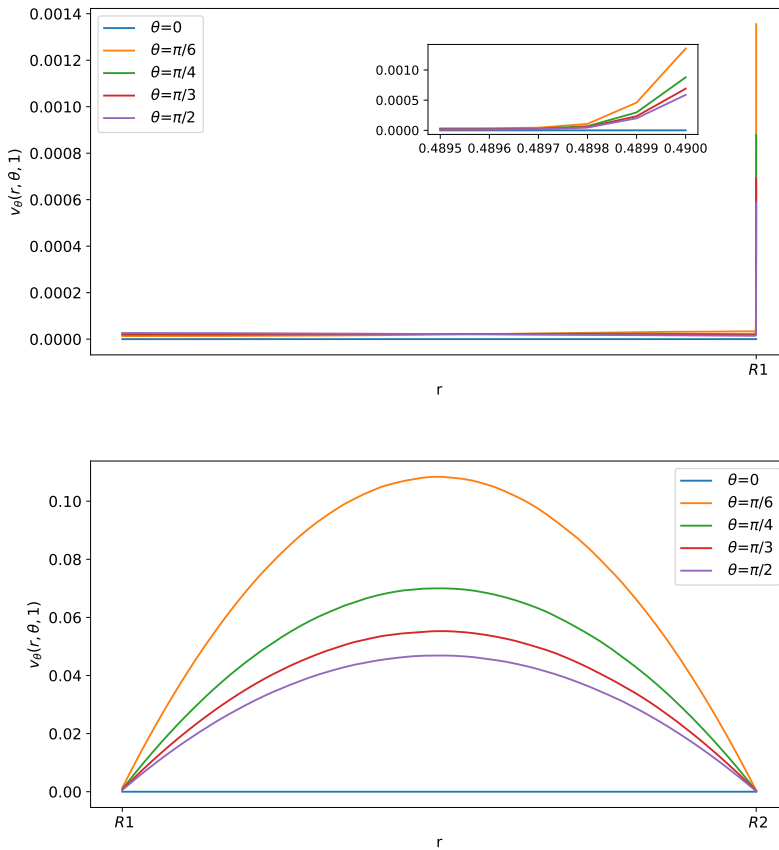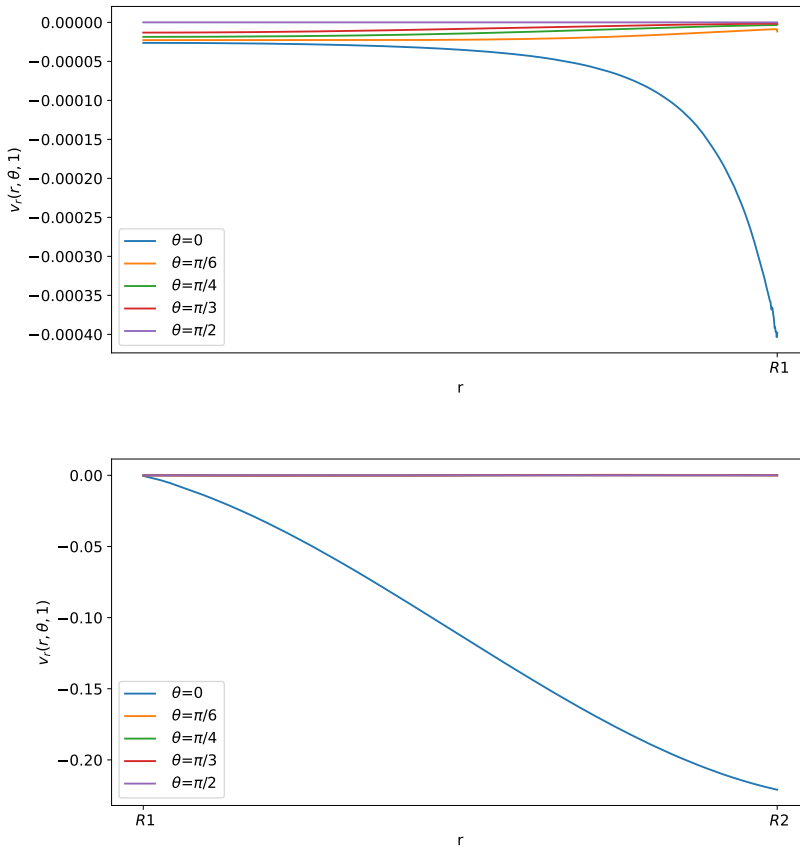
Fig. 5 Tangential component of the velocity in mm/s with respect to the radius at different angles at $t = 1$ s. The first graph corresponds to the tangential velocity in the LC (porous part), and the second corresponds to the tangential velocity in the SCS (free-fluid region).

numerical stabilization parameters are estimated as $\gamma_2 = 0$, while $\gamma_1 = 300$ in Ω^S and $\gamma_1 = 10^6$ in Ω^B.

In Figure 5, Figure 6 and Figure 7, we can see the tangential and radial velocity, and the shear stress, respectively. We can see that the results are very similar to the ones explicitly in Section 2.4: in order to remove some small oscillations in the internal velocity near R_1, we needed to use a finer mesh, which meant a greater computational cost for every time step. We can do only a qualitative comparison between the numerical solution of this section and the explicit solution in Section 2.4 because we do not have available and precise physiological data of the lymph node and we have an error in both cases: in the explicit result from the truncation of the sum, and here due to the finite element approximation. Qualitatively, we have the same behavior and values here and in the explicit result.

Fig. 6 Normal component of the velocity in mm/s with respect to the radius at different angles at $t = 1$ s. The first graph corresponds to the tangential velocity in the LC (porous part), and the second corresponds to the tangential velocity in the SCS (free-fluid region).

3.2 Numerical results

In this Section we want to show a more complete numerical simulation using the method given in Section 3.

We use a spherical idealized 2D geometry with the same parameters given in Section 2.2; hence we suppose that the permeability tensor $\mathbf{K}$ is homogeneous and constant (this is not a limiting assumption, see [4, 13, 18]) and the same with the slip tensor $\mathbf{B} = \beta\mathbf{I}$. Moreover, we add to the simulation domain a part to the inlet and outlet lymphatic vessel (see Figure 10 and Figure 8).

As we mention in Section 2.2, more than 90% of the lymph takes a peripheral path; the lymph that enters in the LC does not remain in the LC but gets out due to the incompressibility of the lymph, because we are not taking into account the fluid exchange behavior given by the blood vessels inside the LN.
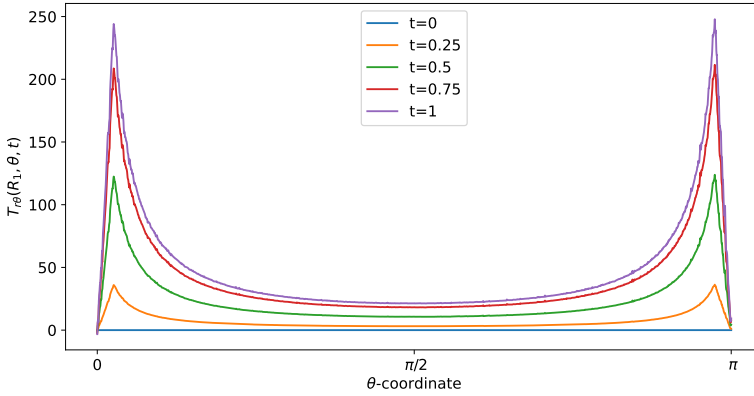
Fig. 7 Shear stress in mPa with respect to the polar coordinates calculated at a fixed radius $r = R_1$ in different times.

The inlet condition is imposed in the upper lymphatic vessel as a uniform pulsatile flow in the y direction with the equation (27).

For the outlet condition, we need to fix the stress. For clarity and for a simpler interpretation, we fix the pressure $\bar{p}(t)$ in this way:

$$\left[\int_{\Gamma_N^S} \mathbf{T}\boldsymbol{w} \cdot \boldsymbol{n}dS\right]_{|\bar{p}} = \left[\int_{\Gamma_N^S} \left(-p\mathbf{I} + \mu\left[\nabla\boldsymbol{v} + \nabla\boldsymbol{v}^T\right]\right)\boldsymbol{w} \cdot \boldsymbol{n}dS\right]_{|\bar{p}} =$$
$$= \int_{\Gamma_N^S} \left(-\bar{p}\mathbf{I} + \mu\left[\nabla\boldsymbol{v} + \nabla\boldsymbol{v}^T\right]\right)\boldsymbol{w} \cdot \boldsymbol{n}dS.$$

We use the numerical parameters given in Section 3.1. In Figure 8, we can see the pressure distribution in the LN with $\bar{p} = 6.18 \times 10^5 f(t)$ mPa ($= 6.3$ cmH$_2$O as the inferior limit in the range of pressure found in [41] and as in the explicit results in Section 2.4), where $f(t)$ is the one given by the equation (41). As we can see, the pressure distribution is similar to the one in Figure 1 and it is in range with the corresponding results. If one has $\bar{p} = 4 \times 10^5 f(t)$ mPa ($= 3$ mmHg as in [13]), the behavior of the pressure is similar to the one showed in Figure 8 (so that we omit the picture), with a range of values comparable to [13].

In Figure 9, we can see the shear stress over time (in mPa). At time $t = 1$ s, we have the maximum value of the velocity (and, consequently, of the shear stress) and the shear stress is similar to the one found in the explicit result (the blue curve with $v_{in} \approx 0.22$ plotted in Figure 2), that is in range with the values found in [10, 13].

We can see the norm and the velocity behavior in more details in Figure 10. The tangential velocity (the most relevant one) is shown in Figure 11. As expected, the maximum velocity is in the SCS near the inlet and the outlet
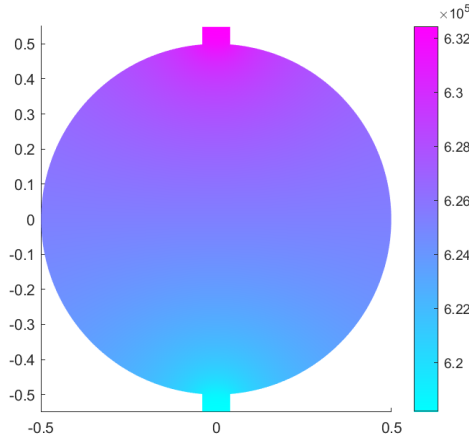
**Fig. 8** Pressure distribution in mPa with fixed pressure $\bar{p} = 6.18 \times 10^5$ mPa at outlet.
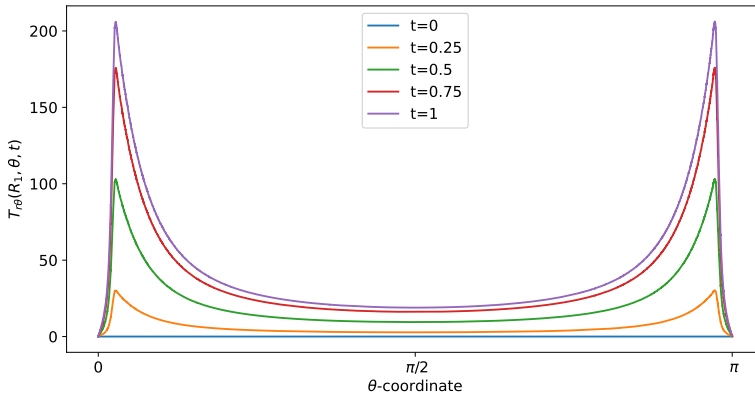
Fig. 9 Shear stress in mPa with respect to the polar angle ($\theta = 0$ near the inlet flow and $\theta = \pi$ near the outlet flow) calculated at different times.

region. In particular, we can see that the maximum velocity is between the connections of the SCS with the afferent/efferent vessel; then the velocity decrease with respect to the polar coordinate θ, reaching the minimum at $\theta = \pi/2$. Moreover, even if we do not impose the outlet velocity equal to the inlet one, we have that this is true due to the incompressibility; hence our assumption used to find the explicit solution is not too limiting in this case.

Conclusion

We proposed a model that describes the pulsatile lymph flow inside a simplified spherical lymph node (LN), using the Darcy-Brinkman equation to describe
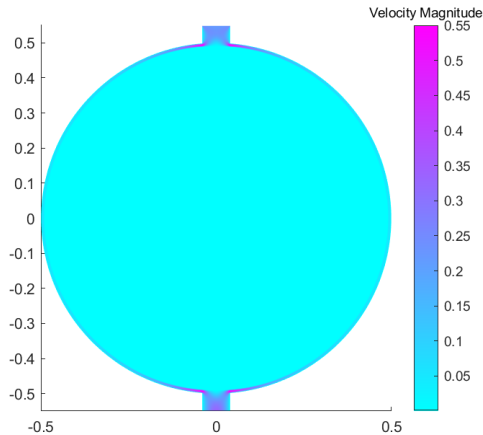
Fig. 10 Velocity magnitude in mm/s at $t = 1\,\mathrm{s}$ (maximum velocity).

the lymph flow in the lymphoid compartment (LC, the porous part) and the Stokes equation to describe the flow inside the subcapsular sinus (SCS, the free fluid region). We found the explicit solution in terms of Gegenbauer polynomials and we showed the trend of the velocity, the pressure and the shear stress inside the LN; after that, we used this explicit solution to validate the numerical simulations of the model. Finally, we performed a more general numerical simulation with finite elements.

This model allows to better understand the fluid behavior inside the LN and how it changes with respect to time. The results obtained by our model are in agreement with the literature [10, 13–15, 18]. We remark that the Ochoa-Tapia boundary condition minimally affects the fluid behavior in the SCS. Still, it affects the flow in the LC, inducing a velocity profile which is not smooth at the interface between the LC and SCS regions.

Particular attention was paid to the shear stress, because a lot of biological phenomena in the LN depend on it. Among them is the cell adhesion to the exterior of the LC, which is proportional to the shear stress: this is important because inside the LC there is a connection between the lymphatic system and the blood system, and some cells can get access from here to the blood circulation (for instance, tumor cells [10]). Moreover, shear stress drives drug delivery and can affect pathologies like B-cell lymphoma [8, 9]. In our model we found that the shear stress is higher near the inlet and the outlet regions, and decreases with respect to the polar angle θ, reaching the minimum at $\theta = \pi/2$; hence we believe that the majority of the cell adhesion is located near these two critical regions, which are the connections of the SCS with the afferent/efferent vessels.

Let us now make some considerations that can be interesting to improve the model in future. Here we have proposed to use a spherical geometry, but in general the LNs have a spheroidal shape [13–15, 17].
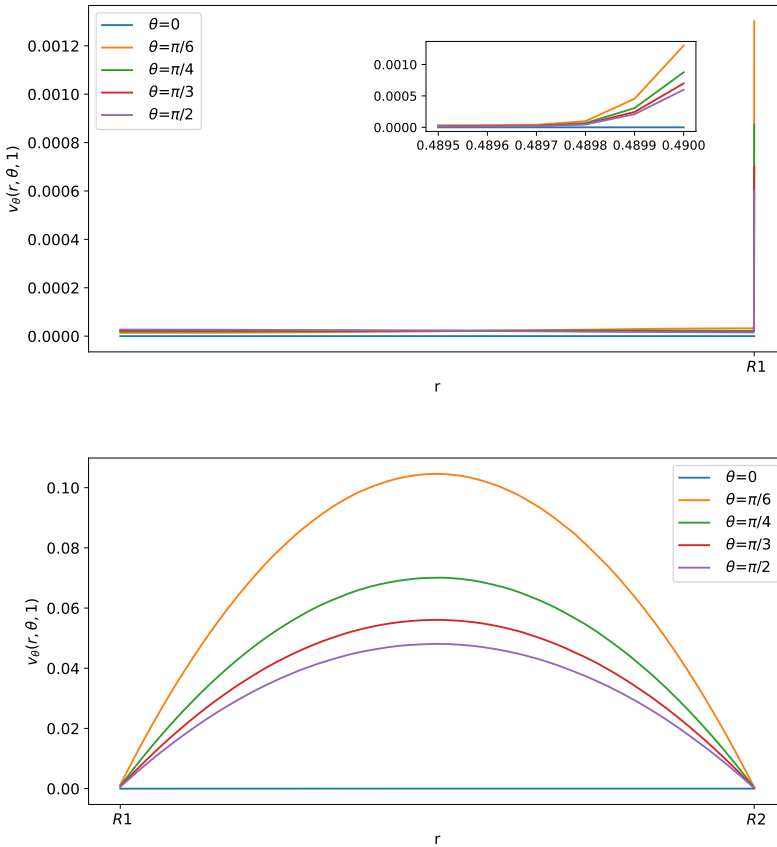
Fig. 11 Tangential component of the velocity in mm/s with respect to the radius at different angles at $t = 1$ s. The first graph corresponds to the tangential velocity in the LC (porous part), and the second corresponds to the tangential velocity in the SCS (free-fluid region).

For simplicity, we did not take into account the fluid exchange inside the LN between the lymph in the fibroblastic reticular cells FRC and the blood in the capillaries, although it is important for the fluid regulation of the LN [47]; a further extension of this work could take this phenomenon into account.

Moreover, in order to close our model and to find the unknown constants in the explicit solution, we used the Ochoa-Tapia boundary conditions, although other boundary conditions can be taken into consideration. For instance, a common choice is to impose the continuity also of the shear stress at the interface, which is tantamount to choose $\beta = 0$ in eq. (40). Using the same technique, one can address the more general conditions given in [48, 49], where there is a discontinuity also of the tangential velocity and the normal stress.

Another interesting and important extension of this model would be to couple the flow in the lymph node with the flow in the lymphangion, in order

to have more realistic time pulsation and see how the lymph node affects and regulates the global lymph circulation [20, 39, 40].

Declarations

Data sharing not applicable to this article as no datasets were generated or analysed during the current study.

Acknowledgement

References

[1] Arasa, J., Collado-Diaz, V., Halin, C.: Structure and immune function of afferent lymphatics and their mechanistic contribution to dendritic cell and T cell trafficking. Cells **10**(5), 1269 (2021)

[2] Roozendaal, R., Mebius, R.E., Kraal, G.: The conduit system of the lymph node. International immunology **20**(12), 1483–1487 (2008)

[3] Grebennikov, D., Van Loon, R., Novkovic, M., Onder, L., Savinkov, R., Sazonov, I., Tretyakova, R., Watson, D.J., Bocharov, G.: Critical issues in modelling lymph node physiology. Computation **5**(1), 3 (2016)

[4] Savinkov, R., Kislitsyn, A., Watson, D.J., van Loon, R., Sazonov, I., Novkovic, M., Onder, L., Bocharov, G.: Data-driven modelling of the FRC network for studying the fluid flow in the conduit system. Engineering Applications of Artificial Intelligence **62**, 341–349 (2017). https://doi.org/10.1016/j.engappai.2016.10.007

[5] Novkovic, M., Onder, L., Bocharov, G., Ludewig, B.: Topological structure and robustness of the lymph node conduit system. Cell Reports **30**(3), 893–904 (2020)

[6] von Andrian, U.H., Mempel, T.R.: Homing and cellular traffic in lymph nodes. Nature Reviews Immunology **3**(11), 867–878 (2003)

[7] O'Melia, M.J., Lund, A.W., Thomas, S.N.: The biophysics of lymphatic transport: Engineering tools and immunological consequences. Iscience **22**, 28–43 (2019)

[8] Apoorva, F., Loiben, A.M., Shah, S.B., Purwada, A., Fontan, L., Goldstein, R., Kirby, B.J., Melnick, A.M., Cosgrove, B.D., Singh, A.: How biophysical forces regulate human B cell lymphomas. Cell reports **23**(2), 499–511 (2018). https://doi.org/10.1016/j.celrep.2018.03.069

[9] Lamaison, C., Latour, S., Hélaine, N., Morvan, V.L., Monvoisin, C., Mahouche, I., Dussert, C., Dessauge, E., Pangault, C., Seffals, M., Broca-Brisson, L., Alessandri, K., Soubeyran, P., Mourcin, F., Nassoy, P., Recher, G., Tarte, K., Bresson-Bepoldin, L.: Stromal cells regulate malignant B-cell spatial organization, survival, and drug response in a new 3D model mimicking lymphoma tumor niche. bioRxiv (2020). https://doi.org/10.1101/2020.10.17.343657

[10] Birmingham, K.G., O'Melia, M.J., Bordy, S., Aguilar, D.R., El-Reyas, B., Lesinski, G., Thomas, S.N.: Lymph node subcapsular sinus microenvironment-on-a-chip modeling shear flow relevant to lymphatic metastasis and immune cell homing. Iscience **23**(11), 101751 (2020)

[11] Permana, A.D., Nainu, F., Moffatt, K., Larrañeta, E., Donnelly, R.F.: Recent advances in combination of microneedles and nanomedicines for lymphatic targeted drug delivery. Wiley Interdisciplinary Reviews: Nanomedicine and Nanobiotechnology **13**(3), 1690 (2021)

[12] Novkovic, M., Onder, L., Cheng, H.-W., Bocharov, G., Ludewig, B.: Integrative computational modeling of the lymph node stromal cell landscape. Frontiers in Immunology, 2428 (2018)

[13] Jafarnejad, M., Woodruff, M.C., Zawieja, D.C., Carroll, M.C., Moore Jr, J.: Modeling lymph flow and fluid exchange with blood vessels in lymph nodes. Lymphatic research and biology **13**(4), 234–247 (2015)

[14] Cooper, L.J., Heppell, J.P., Clough, G.F., Ganapathisubramani, B., Roose, T.: An image-based model of fluid flow through lymph nodes. Bulletin of mathematical biology **78**(1), 52–71 (2016)

[15] Cooper, L., Zeller-Plumhoff, B., Clough, G., Ganapathisubramani, B., Roose, T.: Using high resolution X-ray computed tomography to create an image based model of a lymph node. Journal of Theoretical Biology **449**, 73–82 (2018)

[16] Tretiakova, R., Setukha, A., Savinkov, R., Grebennikov, D., Bocharov, G.: Mathematical modeling of lymph node drainage function by neural network. Mathematics **9**(23), 3093 (2021)

[17] Giantesio, G., Girelli, A., Musesti, A.: A model of the pulsatile fluid flow in the lymph node. Mechanics Research Communications **116**, 103743 (2021)

[18] Shanti, A., Samara, B., Abdullah, A., Hallfors, N., Accoto, D., Sapudom, J., Alatoom, A., Teo, J., Danti, S., Stefanini, C.: Multi-compartment 3D-cultured organ-on-a-chip: towards a biomimetic lymph node for drug development. Pharmaceutics **12**(5), 464 (2020)

[19] Shanti, A., Teo, J., Stefanini, C.: In vitro immune organs-on-chip for drug development: a review. Pharmaceutics **10**(4), 278 (2018)

[20] Moore Jr, J.E., Bertram, C.D.: Lymphatic system flows. Annual review of fluid mechanics **50**, 459–482 (2018)

[21] Mozokhina, A., Savinkov, R.: Mathematical modelling of the structure and function of the lymphatic system. Mathematics **8**(9), 1467 (2020)

[22] Happel, J., Brenner, H.: Low Reynolds Number Hydrodynamics: with Special Applications to Particulate Media. Martinus Nijhoff Publishers, The Hague (1983)

[23] Hecht, F.: New development in FreeFem++. J. Numer. Math. **20**(3-4), 251–265 (2012)

[24] Nield, D.A.: Modelling fluid flow and heat transfer in a saturated porous medium. Journal of applied mathematics and decision sciences **4**(2), 165–173 (2000)

[25] Haberman, W.L., Sayre, R.M.: Motion of rigid and fluid spheres in stationary and moving liquids inside cylindrical tubes. Technical report, David Taylor Model Basin Washington DC (1958)

[26] Kislitsyn, A., Savinkov, R., Novkovic, M., Onder, L., Bocharov, G.: Computational approach to 3D modeling of the lymph node geometry. Computation **3**(2), 222–234 (2015)

[27] Ulvmar, M.H., Werth, K., Braun, A., Kelay, P., Hub, E., Eller, K., Chan, L., Lucas, B., Novitzky-Basso, I., Nakamura, K., *et al.*: The atypical chemokine receptor CCRL1 shapes functional CCL21 gradients in lymph nodes. Nature immunology **15**(7), 623–630 (2014)

[28] Das, S., Sarrou, E., Podgrabinska, S., Cassella, M., Mungamuri, S.K., Feirt, N., Gordon, R., Nagi, C.S., Wang, Y., Entenberg, D., *et al.*: Tumor cell entry into the lymph node is controlled by CCL1 chemokine expressed by lymph node lymphatic sinuses. Journal of Experimental Medicine **210**(8), 1509–1528 (2013)

[29] Zhang, Z., Procissi, D., Li, W., Kim, D.-H., Li, K., Han, G., Huan, Y., Larson, A.C.: High resolution MRI for non-invasive mouse lymph node mapping. Journal of immunological methods **400**, 23–29 (2013)

[30] Adair, T.H., Guyton, A.C.: Modification of lymph by lymph nodes. II. Effect of increased lymph node venous blood pressure. American Journal of Physiology-Heart and Circulatory Physiology **245**(4), 616–622 (1983)

[31] Adair, T.H., Guyton, A.C.: Modification of lymph by lymph nodes. III. Effect of increased lymph hydrostatic pressure. American Journal of Physiology-Heart and Circulatory Physiology **249**(4), 777–782 (1985)

[32] Blatter, C., Meijer, E.F., Nam, A.S., Jones, D., Bouma, B.E., Padera, T.P., Vakoc, B.J.: In vivo label-free measurement of lymph flow velocity and volumetric flow rates using Doppler optical coherence tomography. Scientific reports **6**(1), 1–10 (2016)

[33] Ochoa-Tapia, J.A., Whitaker, S.: Momentum transfer at the boundary between a porous medium and a homogeneous fluid I. Theoretical development. International Journal of Heat and Mass Transfer **38**(14), 2635–2646 (1995)

[34] Tan, H., Pillai, K.M.: Finite element implementation of stress-jump and stress-continuity conditions at porous-medium, clear-fluid interface. Computers & Fluids **38**(6), 1118–1131 (2009)

[35] Ochoa-Tapia, J.A., Whitaker, S.: Momentum transfer at the boundary between a porous medium and a homogeneous fluid II. Comparison with experiment. International Journal of Heat and Mass Transfer **38**(14), 2647–2655 (1995)

[36] Prakash, J.: Hydrodynamic mobility of a porous spherical particle with variable permeability in a spherical cavity. Microsystem Technologies **26**(8), 2601–2614 (2020)

[37] Abramowitz, M., Stegun, I.A.: Handbook of Mathematical Functions with Formulas, Graphs, and Mathematical Tables vol. 55. US Government printing office, Washington, D.C. (1964)

[38] Zlatanovski, T.: Axisymmetric creeping flow past a porous prolate spheroidal particle using the Brinkman model. The Quarterly Journal of Mechanics and Applied Mathematics **52**(1), 111–126 (1999)

[39] Bertram, C., Macaskill, C., Davis, M., Moore, J.: Valve-related modes of pump failure in collecting lymphatics: numerical and experimental investigation. Biomechanics and modeling in mechanobiology **16**(6), 1987–2003 (2017)

[40] Bertram, C., Macaskill, C., Moore, J.: Inhibition of contraction strength and frequency by wall shear stress in a single-lymphangion model. Journal of biomechanical engineering **141**(11) (2019)

[41] Bouta, E.M., Wood, R.W., Brown, E.B., Rahimi, H., Ritchlin, C.T., Schwarz, E.M.: In vivo quantification of lymph viscosity and pressure in lymphatic vessels and draining lymph nodes of arthritic joints in mice.

The Journal of physiology **592**(6), 1213–1223 (2014)

[42] Jenkins, E.W., John, V., Linke, A., Rebholz, L.G.: On the parameter choice in grad-div stabilization for the Stokes equations. Advances in Computational Mathematics **40**(2), 491–516 (2014)

[43] Neilan, M., Zytoon, A.: Connection between grad-div stabilized Stokes finite elements and divergence-free Stokes finite elements. International journal of numerical analysis and modeling **17**(6) (2020)

[44] Qin, Y., Hou, Y., Huang, P., Wang, Y.: Numerical analysis of two grad–div stabilization methods for the time-dependent Stokes/Darcy model. Computers & Mathematics with Applications **79**(3), 817–832 (2020)

[45] Rong, Y., Fiordilino, J.A.: Numerical analysis of a BDF2 modular grad–div stabilization method for the Navier–Stokes equations. Journal of Scientific Computing **82**(3), 1–22 (2020)

[46] Xie, X., Xu, J., Xue, G.: Uniformly-stable finite element methods for Darcy-Stokes-Brinkman models. Journal of Computational Mathematics, 437–455 (2008)

[47] Tobbia, D., Semple, J., Baker, A., Dumont, D., Semple, A., Johnston, M.: Lymphedema development and lymphatic function following lymph node excision in sheep. Journal of vascular research **46**(5), 426–434 (2009)

[48] Angot, P., Goyeau, B., Ochoa-Tapia, J.A.: Asymptotic modeling of transport phenomena at the interface between a fluid and a porous layer: Jump conditions. Physical Review E **95**(6), 063302 (2017)

[49] Angot, P.: Well-posed Stokes/Brinkman and Stokes/Darcy coupling revisited with new jump interface conditions. ESAIM: Mathematical Modelling and Numerical Analysis **52**(5), 1875–1911 (2018)